Full Length Article

Tuning graphitic carbon nitride (g-C$_3$N$_4$) electrocatalysts for efficient oxygen evolution reaction (OER)

André Torres-Pinto [a,b,c], Aida M. Díez [c,*], Cláudia G. Silva [a,b], Joaquim L. Faria [a,b], M. Ángeles Sanromán [c], Adrián M.T. Silva [a,b,*], Marta Pazos [c]

[a] LSRE-LCM - Laboratory of Separation and Reaction Engineering – Laboratory of Catalysis and Materials, Faculty of Engineering, University of Porto, Rua Dr. Roberto Frias, 4200-465 Porto, Portugal
[b] ALiCE - Associate Laboratory in Chemical Engineering, Faculty of Engineering, University of Porto, Rua Dr. Roberto Frias, 4200-465 Porto, Portugal
[c] CINTECX, Universidade de Vigo, BIOSUV Group, Department of Chemical Engineering, 36310 Vigo, Spain

ARTICLE INFO

ABSTRACT

Nowadays, energy conversion and storage technologies are essential research topics due to the necessity of more sustainable processes. Specifically, water splitting is highly affected by slow kinetics and limited knowledge of the oxygen evolution reaction (OER). This work envisages the preparation of graphitic carbon nitride (g-C$_3$N$_4$) electrocatalysts for efficient OER by a facile one-pot method. The impact of the preparation temperature (450–650 °C) of g-C$_3$N$_4$ was assessed for the first time on water splitting processes and explained by different characterisation techniques. The unique crystal structure, surface chemistry, and electronic properties of the material prepared at 550 °C lead to a remarkable OER efficiency, with an overpotential of 355 mV at 10 mA cm^{-2} and a Tafel slope of 46.8 mV dec^{-1}. Interestingly, three major differences were observed when comparing the material prepared at 550 °C with those obtained at other temperatures: the reduced structural distortion, the superior composition in oxygen and the presence of terminal functional groups. Also, compared to other metal-free g-C$_3$N$_4$ electrocatalysts reported in the literature, we achieved lower Tafel slope values without additional post-treatments or co-catalysts. Hence, for the first time a metal-free catalyst defeats benchmark IrO$_2$. The prepared electrodes were stable for up to 45 h, even when increasing the applied current density to 100 mA cm^{-2} for 15 h. Thus, this work provides a simple route for the fabrication of highly-efficient and long-lasting electrocatalysts for a remarkable OER performance.

1. Introduction

Currently, there is an increasing demand for sustainable energy conversion and storage technologies owing to the environmental pollution issues caused by fossil fuels [1,2]. Thus, research is being directed towards developing alternative sources of energy. In particular, the water splitting reaction can be a promising solution for the energy sector [3]. Electrochemical or electrocatalytic setups can be efficient to promote overall water splitting. The primary operational challenge on these systems lies on the energy-demanding and rate-limiting step of the oxygen-forming oxidation reaction [4,5].

The oxygen evolution reaction (OER) typically shows a large energy consumption ascribed to the substantially high overpotential required

and its slow kinetic mechanism due to the four-electron transfer reaction [4–6]. Therefore, it is imperative to prepare efficient electrocatalysts to bypass these drawbacks, on the way to attain an efficient overall water splitting reaction. The OER performance is related to the intrinsic activity of a catalyst, depending on the electrochemically active sites [4]. Several materials have been proposed for OER, such as layered double-hydroxides (LDH), metal–organic frameworks (MOFs) or chalcogenides and perovskites [7–11]. These metal-based catalysts have limitations such as the need for critical raw materials and their high processing costs [12]. Moreover, the possibility of metal leaching as a serious environmental threat hinders their applicability and industrialisation in some fields [13,14].

Carbon-derived electrocatalysts are being intensively researched to

---

overcome these drawbacks [15]. For instance, graphitic carbon nitride (g-C$_3$N$_4$, herein labelled as CN), mainly employed in heterogeneous photocatalysis [16–18], has emerged as a promising material for electrocatalytic water splitting [19–22]. Thus, this material can effectively catalyse the water oxidation process with relatively low energy consumption, owing to its unique electronic structure[23]. Many works have combined CN with other metal-based materials creating bifunctional electrocatalysts [24–26], such as a lanthanum-strontium-titanium perovskite coupled to CN which achieved a substantially low overpotential of 62 mV at 10 mA cm^{-2} compared to the 178 mV of the respective bare CN material [27]. Another work combined CN with a cobalt-ferrite nanocomposite and explored the photocatalytic ability of CN, fashioning a photoanode that allowed for an OER overpotential of 200 mV at 10 mA cm^{-2} under white LED illumination (in comparison to 290 mV for the same current density in dark conditions) [28].

As reported, CN-derived electrocatalysts are often combined with metal-based materials for increased electrochemical performance. In the present work, we synthesised several metal-free CN catalysts for the first time under different preparation temperatures and evaluated their OER performance. Hybrids of metal-free CN catalysts have been previously designed for OER to improve the overall water splitting efficiency, but their preparation procedure, which requires several synthesis stages or combination with other materials, compromises the straightforwardness, environmentally green character, and inexpensiveness of the proposed system [20]. Herein, we demonstrate the optimisation of a simple thermal preparation method to obtain CN electrocatalysts with low overpotentials (reaching as low as 355 mV at 10 mA cm^{-2}) and high electrochemical efficiency (with a Tafel slope of 46.8 mV dec^{-1}). Additionally, this electrocatalyst showed an outstanding stability during 45 h. Furthermore, the catalysts were exhaustively characterised to understand the implications of this simple and innovative thermal treatment on the synergy between physicochemical properties and electrocatalytic activity of these materials. This investigation is pivotal to comprehend the intrinsic chemical modifications essential to achieve an optimal CN electrocatalyst.

2. Materials and methods

2.1. Preparation of CN electrodes

The CN materials were prepared following a procedure adapted from our previous report dealing with its use as photocatalysts [29]. Urea (CH$_4$N$_2$O, 99.3 %, obtained from Alfa Aesar) was employed as a precursor and heated in semi-closed quartz crucibles in a microwave muffle furnace (Phoenix, CEM Corporation). Two heating stages were carried out, the first by heating up to 450 °C at 2 °C min^{-1} and maintaining the temperature for 30 min. Then, the temperature was either maintained for 90 min (to prepare CN–450) or increased at 2 °C min^{-1} until 500, 550, 600 or 650 °C and maintained for 60 min to obtain CN-500, CN-550, CN-600 or CN-650, respectively. The resulting powders were washed with distilled water, filtered, and dried overnight.

The electrodes were prepared by spreading a previously prepared slurry of the CN catalyst onto a nickel foam (1 cm × 1 cm) obtained from Goodfellow. Briefly, 3 mg of catalyst were dispersed in a mixture of 1000 μL of absolute ethanol (≥99.8 %, obtained from Sigma-Aldrich) and 50 μL of Nafion (Nafion™ perfluorinated resin solution, from Sigma-Aldrich). After sonication, selected volumes, according to the desired catalyst loading, were deposited dropwise onto the nickel foam support to prepare the working electrodes. Iridium oxide (IrO$_2$, 99.9 %, obtained from Alfa Aesar) was employed as a reference electrode for OER, prepared by using the same deposition method.

2.2. Materials characterisation

Scanning electron microscopy (SEM) analyses were carried out using a JEOL JSM 6010LA electron microscope coupled with an electron-dispersive spectroscopy (EDS) microanalysis system, while transmission electron microscopy (TEM) was performed on a JEOL JEM-1400 Flash instrument with an acceleration voltage of 120 kV. X-ray diffraction (XRD) patterns from powdered samples were collected using a PANalytical X'Pert Pro diffractometer, equipped with a PW3050/60 (Theta/2Theta) goniometer and monochromatic CuKα$_{1,2}$ radiation (1.5406 Å, 40 kV and 30 mA), in the 2θ angular range of 5° to 70° using a continuous scan mode at a speed of 0.0175° s^{-1}. Raman spectroscopy was performed in an FT-Raman RAM II dispersive Raman spectrometer (Bruker) equipped with a high-resolution germanium array detector and an Nd-YAG laser source for operation at 1064 nm. Fourier transform infrared (FTIR) measurements were performed on a JASCO FT/IR-6800 spectrometer (JASCO Analytical Instruments, USA) equipped with a MIRacle™ Single Reflection attenuated total reflectance ZnSe crystal plate accessory (PIKE Technologies, USA). Multipoint analysis of N$_2$ adsorption–desorption isotherms at − 196 °C was performed on a Quantachrome Autosorb iQ apparatus, with the samples being degassed under vacuum for 12 h at 150 °C prior to analysis. The specific surface area was calculated by the Brunauer-Emmett-Teller method (S_{BET}), while the pore size distribution was obtained by the Barrett-Joyner-Halenda method.

X-ray photoelectron spectroscopy (XPS) was performed using a Thermo Scientific NEXSA instrument equipped with an electron flood gun to minimise surface charging. XPS analyses were carried out using a monochromatic Al-Kα radiation at 1486.6 eV in a Constant Analyser Energy mode (CAE) with a 100-eV pass energy for survey spectra and 20-eV pass energy for high-resolution spectra. Elemental analysis (EA) was carried out by combustion at 1050 °C in a Vario Micro Cube analyser (Elementar, GmbH) to determine C, N and H content and by pyrolysis, at 1450 °C using a Rapid Oxy Cube analyser (Elementar, GmbH) to analyse O content. The diffuse reflectance UV–Vis spectroscopy (DRS) was performed on a JASCO V 560 spectrophotometer equipped with an integrating sphere attachment (JASCO ISV-469). Solid-phase and steady-state photoluminescence (PL) measurements were obtained using a spectrofluorometer at room temperature on a JASCO (FP 82000) fluorescence spectrometer with a 150 W Xenon lamp as a light source - both excitation and emission bandwidth were fixed at 2.5 nm, the excitation wavelength established at 270 nm and emission detection range between 390 and 700 nm.

2.3. Electrochemical experiments

The OER experiments were performed with an electrochemical workstation (Autolab PGSTAT302N, Metrohm) equipped with a FRA32M frequency response analyser. The electrochemical cell consisted of a three-electrode setup, using saturated calomel as the reference electrode and platinum wire (from Alfa Aesar) as the counter electrode. The working electrodes were prepared as described previously. The electrolytes were aqueous solutions of 0.5 M H$_2$SO$_4$ (95 %, VWR Chemicals), 1.0 M NaOH (98.5 %, VWR Chemicals) or 0.5 M Na$_2$SO$_4$ (≥99.0 %, Sigma–Aldrich).

Cyclic voltammetry (CV) was carried out at a scan rate of 5 mV s^{-1}. Electrochemical impedance spectroscopy (EIS) was performed at the overpotential (η_{10}) in the frequency range of 10^6 to 10^{-2} Hz, with a 10 mV sinusoidal perturbation. The double-layer capacitance (C_{dl}) was estimated after performing cyclic voltammograms at various scan rates (5, 10, 25, 50, 100, 200, 400 and 800 mV s^{-1}) and collected in the non-Faradaic potential range between 1.00 and 1.15 V vs RHE. The C_{dl} corresponds to the slope of the absolute difference between anodic and cathodic current densities at 1.07 V vs RHE with the scan rates. The electrochemical surface area (ECSA) was determined by dividing the obtained C_{dl} by the capacitance of a model catalyst with a unitary surface area (generally, 40 μF cm^{-2}). The stability of the catalyst was evaluated by chronopotentiometry at constant current densities of 10, 50 and 100 mA cm^{-2}. All recorded potentials were converted using the reversible hydrogen electrode (RHE) as a reference.

3. Results and discussion

3.1. Characterisation of CN materials

3.1.1. SEM and TEM

The morphology of the prepared materials was examined through SEM and TEM (Fig. 1). The images portrayed in Fig. 1 depict the layered composition of these materials. The compact nature of the CN nanosheets seems more evident in the case of the materials obtained at lower temperatures. Moreover, increasing the processing temperature induced a pronounced holey formation with seemingly more spaced-out layers. This distortion of the CN layers may promote a higher surface area and greater availability of redox-active sites. Additionally, as observed more easily in TEM there is a higher degree of disruption in the compact layered structure of CN with higher preparation temperatures, *e.g.* CN-450 and CN-500 showing intermingled lamellae-like assemblies, while CN-600 and CN-650 illustrate more fragmented sheets.

3.1.2. XRD

The crystallinity of the CN materials was investigated using XRD. The XRD patterns of the five catalytic materials are given in Fig. 2**a**. CN materials typically show two signals characteristic of their monomeric building blocks (the tri-s-triazine units) [30]. These two peaks are related to the (1 0 0) and (0 0 2) facets and are respectively observed at around 13° and 27°, signalled with dashed lines in Fig. 2**a**, and details of the latter are shown in Table 1. Typically, a higher intensity of an XRD signal is associated with a higher degree of crystallinity of that specific plane. The augmentation of those peaks, easily observed in Fig. 2**a**, is directly related to the preparation temperature and is intricately connected to a stronger presence of crystal structures [31]. The crystallite size (L_c) and interlayer spacing (d) were obtained from Scherrer's equation and Bragg's law, respectively, after a Lorentzian fit of the (0 0 2) peak (Table 1). The deviation of the (0 0 2) reflection is attributed to surface modifications in the graphitic planes of CN, with the more amorphous materials showing a lower peak position. At the same time, a reduced FWHM was observed for higher temperatures, along with a decreased interlayer spacing value from 0.945 Å (CN-450) to 0.824 Å (CN-650), the latter derived from the deviated (0 0 2) reflection. The reduced d-spacing can be attributed to the rearrangement of CN nanosheets, which are formed at higher temperatures as seen by the increased crystallinity (*i.e.*, higher intensity of the (0 0 2) reflection).

The crystallite size is also greatly affected by the preparation temperature, as larger crystals are obtained for higher temperatures (*i.e.*, 1.011 Å for CN-450 and 4.061 Å for CN-650). Moreover, above 550 °C, a higher number of peaks are observed in the diffractograms (Fig. 2**a**), which can be attributed to other crystallite particles or highly–conjugated planes in the polymeric matrix. Particularly, the peaks at 13.7, 17.4, 21.4 and 57.2° are attributed, respectively, to the (1 1 0), (1 0 1), (1 0 1) and (0 0 4) facet orientations [32]. The appearance of these new reflections is related to a rearranged structure of the materials prepared at higher temperatures.

3.1.3. FTIR

FTIR analyses (Fig. 2**b**) were also performed to investigate the overall chemical structure and presence of functional groups in the materials. The prepared materials show the typical spectra of CN materials with a broad band near 3200 cm^{-1} attributed to –OH groups from adsorbed water and to the stretching vibration of N-H$_x$ groups; various medium intensity bands from the range between 1200 and 1600 cm^{-1} assigned to the molecular stretching of carbon–nitrogen bonds; and two more bands near 800 cm^{-1} owed to the aromatic heterocycles [33]. A higher intensity of IR bands is related to a larger availability of the corresponding molecular bonds on the materials' surface. Therefore, in Fig. 2**b** is possible to observe that the overall structure is maintained, but higher temperatures enable a stronger presence of graphitic planes, suggested by the stronger bands at *ca.* 800 cm^{-1}. This increased intensity

can be correlated to a higher polymerisation degree [33,34].

3.1.4. Raman

Raman spectroscopy provides a detailed look into the degree of crystallinity of the prepared materials. The Raman spectra (Fig. 2**c**) were obtained after excitation at 1064 nm (a lower wavelength is inadequate in this case due to the fluorescence interference originated by CN). There is a clear relationship between the preparation temperature and the appearance of peaks, with the materials obtained at higher temperatures showing a larger number of peaks, particularly above 550 °C.

The most prominent peaks found at 706 $\pm$ 2 and 759 $\pm$ 9 cm^{-1} are attributed to triazine ring breathing modes [35], whose intensity increases with the processing temperature. Moreover, the D and G bands observed at 1235 $\pm$ 2 and 1564 $\pm$ 5 cm^{-1}, respectively, are commonly associated with graphitic materials [36] and their surface imperfections. The intensities of both bands increase with the preparation temperature, suggesting an increase in structural defects (D band) and crystallinity (G band). Thus, the modifications seen by Raman spectra are due to the structural changes caused by the processing temperature [37]. The intensity ratios between the D and G bands (I_D/I_G) were also calculated (Fig. 2**c**), this ratio is related to the structural disorder in the materials [35,38], thus proportional to the number of surface defects. The ratio I_D/I_G typically decreases with processing temperature owing to the polymerisation process and increased graphitic structural arrangement; however, for higher temperatures, there is a decrease of sp^2 hybridised moieties and, hence, the I_D/I_G ratio increases [39–42]. Among the prepared materials, CN-550 has the lowest I_D/I_G ratio, implying a reduced level of disorder of graphitic planes, albeit the value being relatively high ($I_D/I_G = 2.51$) there is a considerable number of structural defects.

3.1.5. N$_2$ Adsorption isotherms

The textural properties of the materials were investigated by performing nitrogen adsorption isotherms, presented in Fig. 3**a**. CN materials generally show a type IV adsorption isotherm typical of mesoporous solids (with some microporosity, as depicted from the inset of Fig. 3**a**), with a type H3 hysteresis related to plate-shaped pores formed by a flaky porous structure [43,44]. Pore size distribution can be observed in Fig. 3**b**, showing a bimodal behaviour with smaller mesopores of around 4 nm diameter and a wider mesopore distribution centred at 40 nm.

The specific surface area of the materials was obtained through the BET method, while the average pore size and volume were determined by the BJH approach. As expected by observing the isotherms, the materials prepared at higher temperatures show increasingly higher surface areas and pore volumes (Table 2), while the average pore diameter is not significantly affected. Therefore, increasing the temperature during material preparation promotes the increase on interlayer spacing and a higher degree of exfoliation [34].

3.1.6. CHNS analysis

Elemental analysis was performed to ssess the composition of the prepared materials. The amount of N varied between 58.5 and 61.2 %, while C content was changed from 32.1 to 34.2 %. Both N and C relative contents (seen in Fig. 4) generally increased with the preparation temperature, with decreasing amounts of O and H. The O and H elemental compositions observed in Fig. 4, respectively, were 7.1 and 2.3 % for CN–450 and decreased to 3.0 and 1.6 % for CN-650, while CN-550 showed the highest amount of O at 8.0 %. These variations might be due to the higher polymerisation degree and crystalline structure of the materials prepared at higher temperatures, whereas O/H impurities are removed [31]. Interestingly, the C/N ratio was maintained at 0.55–0.56 for all materials, showing that the thermal treatment has no influence on their relative composition.

3.1.7. XPS

XPS was then performed to characterise the materials' surface regarding their elemental and chemical state information in terms of C,
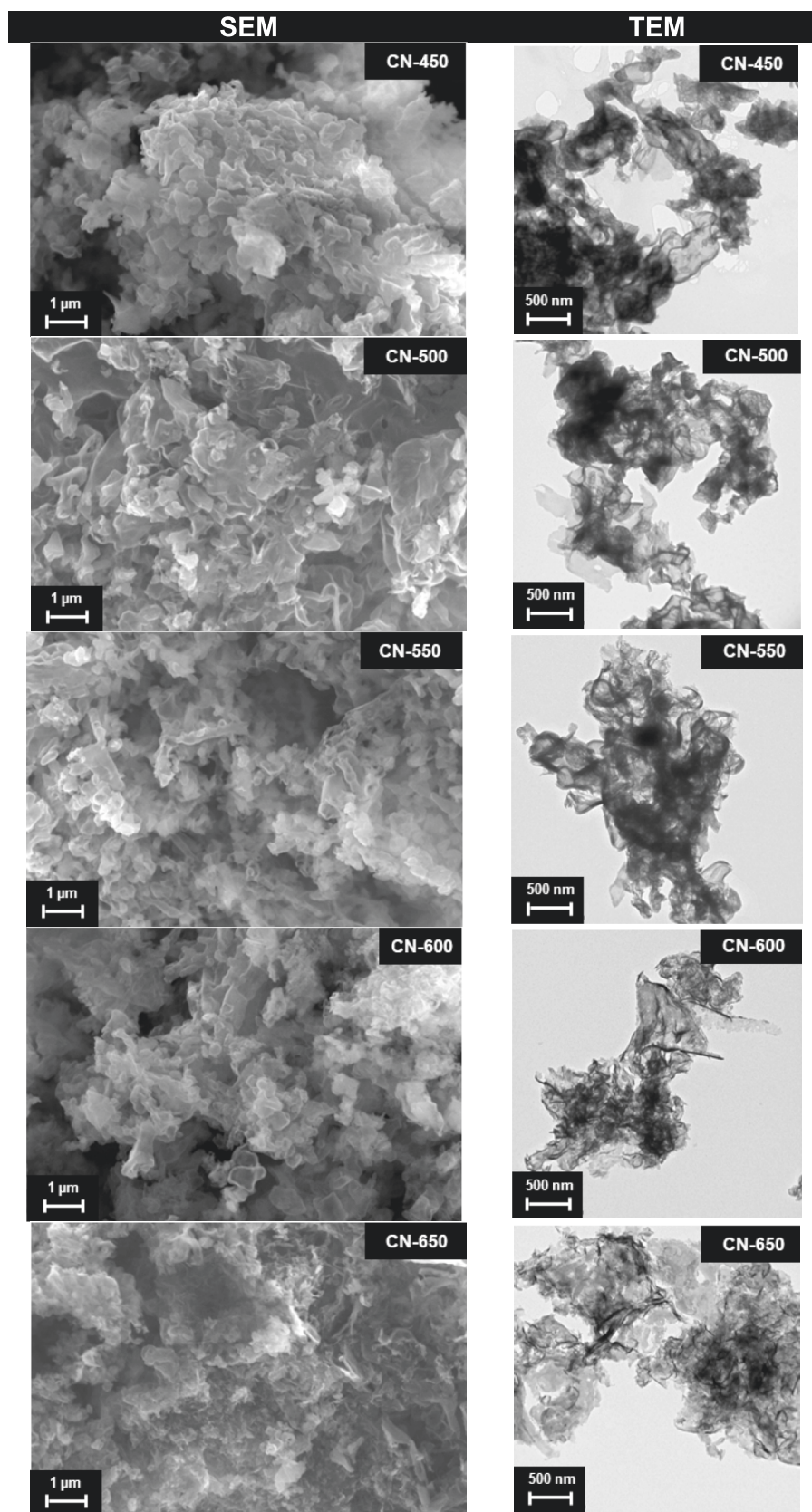
Fig. 1. SEM (left) and TEM (right) images of the CN materials prepared at different temperatures. The number of the image label indicates the temperature (in Celsius) of the second stage heat treatment (e.g., 550 °C in CN-550).
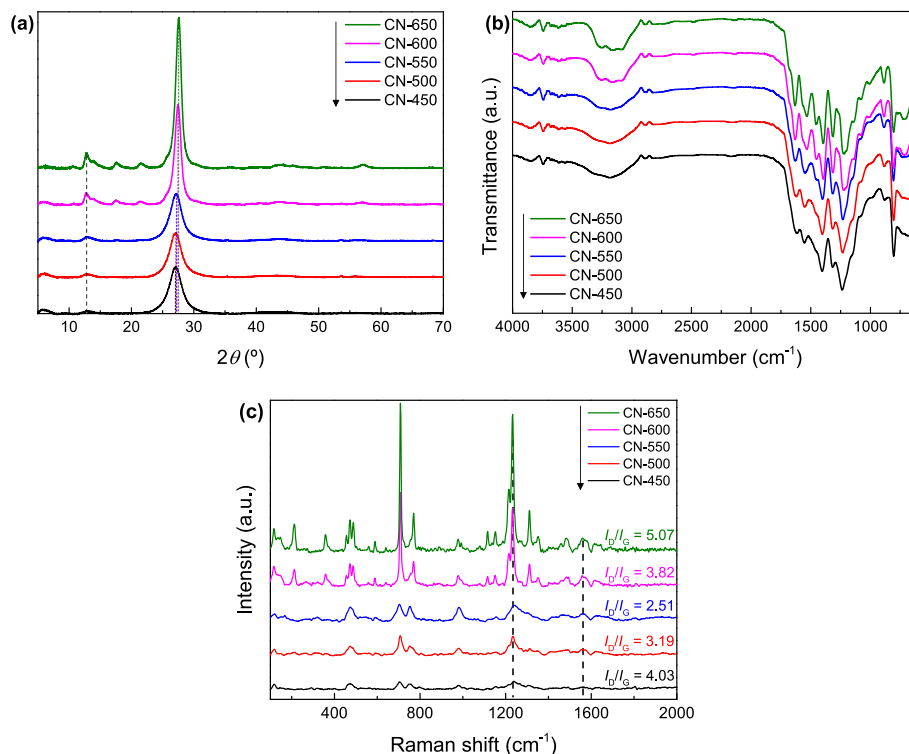
Fig. 2. (a) XRD patterns, **(b)** FTIR and **(c)** Raman spectra of the prepared CN electrocatalysts.

Table 1

XRD results for the (0 0 2) facet of the prepared materials: full width at half maximum (FWHM), crystallite size (L_c) and interlayer spacing (d).

	Position (°)	FWHM (°)	L_c (Å)	d (Å)
CN-450	27.04	2.47	1.011	0.945
CN-500	27.06	2.33	1.092	0.938
CN-550	27.14	2.26	1.192	0.913
CN-600	27.42	1.15	3.032	0.846
CN-650	27.55	1.01	4.061	0.824

N, and O composition. The elemental composition was nearly unchanged with the temperature of the preparation. However, the oxygen content of CN–550 was the highest among all the materials, reaching a total of 8.0 %. The deconvolution of the C 1s, N 1s and O 1s bands was performed and analysed to assess the chemical modifications.

The carbon band was deconvoluted into five peaks (Fig. 5a), from lowest to highest binding energy are attributed to planar C(–N)$_3$ bonds at 284.9 eV, terminal C–NH$_x$ groups at 286.5 eV, graphitic sp^2 hybridised carbon at 288.2 eV (C(–N)$_2$), carbon–oxygen bonds at 289.1 eV and delocalised electronic charges assigned at 293.7 eV [45,46]. It is worth noting that graphitic carbon showed the lowest contribution (51.3 %) for CN-550 compared to the other catalysts (*e.g.*, 60.0 and 64.1 % for CN-450 and CN-650, respectively). At the same time, CN-550 showed the highest contribution of C-NH$_x$ groups (9.8 %) and planar carbon (24.5 %).

Nitrogen was deconvoluted into four peaks, depicted in Fig. 5b: pyridinic (—C—N≡C—) at 398.7 eV, graphitic (N(—C)$_3$) at 399.9 eV; pyrrolic (N—H$_x$) at 401.1 eV and oxidic (N—O) at 404.4 eV [45,46]. The contribution of graphitic nitrogen increased up to 17.5 % for CN-650. On the other hand, pyridinic nitrogen decreased until CN–650 (60.2 %). The

Table 2

Results from nitrogen adsorption–desorption isotherms: specific surface area (S_{BET}), average pore diameter (d_p) and volume (V_p).

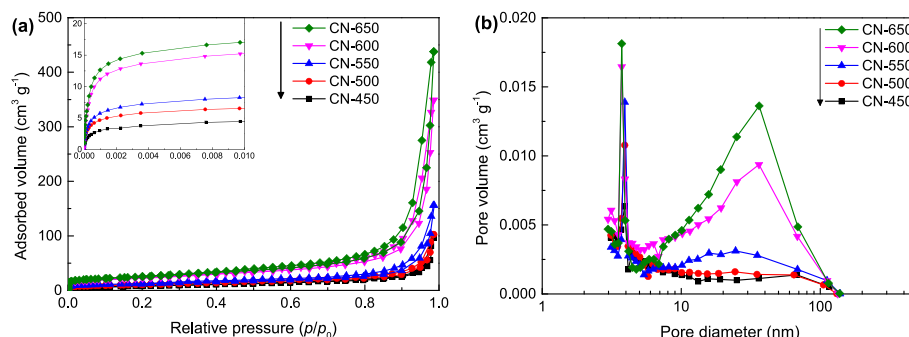| Material	S_{BET} (cm^2 g^{-1})	d_p (nm)	V_p (cm^3 g^{-1})
CN-450	30	3.91	0.144
CN-500	38	3.92	0.151
CN-550	44	3.93	0.223
CN-600	80	3.73	0.535
CN-650	89	3.73	0.675

Fig. 3. (a) Nitrogen adsorption–desorption isotherms with an inset for low p/p_0 values and **(b)** pore size distribution for the prepared CN electrocatalysts.
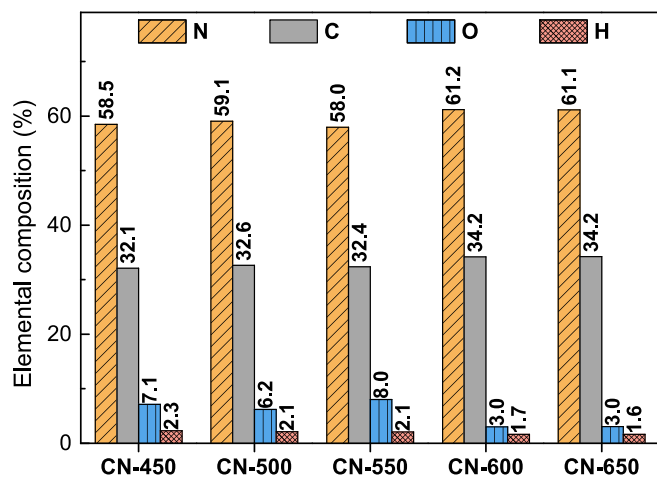
Fig. 4. Elemental composition of the CN electrocatalysts as determined by elemental analysis.

variation of these types of nitrogen leads to the belief that there is a conversion from one to another, meaning the loss of graphitic nitrogen is compensated by the gain of secondary nitrogen bonds [34]. This transformation may be caused from the opening of aromatic rings in the triazine structure, which creates new defects owing to the higher preparation temperature, which is in line with the results observed in Raman through the I_D/I_G ratio augmentation.

Lastly, the oxygen signal was composed of 2 peaks (Fig. 5c): adsorbed —OH groups at 531.9 eV and carbon–oxygen bonds at 533.4 eV [45]. The contribution of the C—O and C═O groups was higher for CN-550 (36.5 %), decreasing for both lower and higher temperatures, which is inversely proportional to the contribution of the hydroxyl/water adsorption peak. Overall, there were no strong variations in peak intensity or binding energies, meaning the chemical states remained relatively identical despite the processing temperature.

3.1.8. UV–vis adsorption

The UV–vis absorption spectra (Fig. 6a) of the materials were measured to ascertain any changes, caused by the preparation temperature, on the chemical nature affecting the optical properties. The materials show minimal visible light absorption above 550 nm, while the maxima are reached for all materials below 390 nm. Higher preparation temperature lead to the extension of the visible light absorption range of the material prepared at 650 °C, showing a moderately high absorption at 440 nm. This enhanced radiative absorption capability is mostly attributed to the stronger presence of spaced-out aromatic heterocycles capable of retaining visible light [34,47].

Tauc's method was used to determine the optical band gap energy levels. The values of E_g (2.70, 2.64, 2.58, 2.53 and 2.47 eV *vs* NHE) decrease with the preparation temperature, proving that the calcination degree is altering the band structure [48]. A narrower band gap can benefit electrochemical applications since less energy is required for charge transfer; however, an overly small band gap energy might also promote faster recombination or unwanted electronic transitions to sink sites. Moreover, the elongation of the absorption spectra can also be attributed to defects associated with transition energy levels that may promote a retained exciton recombination rate and generate trapping sites to facilitate charge carrier transfer [49].

3.1.9. Photoluminescence analysis

The PL emission spectra of the synthesised materials are shown in Fig. 6b, which also includes the normalised PL spectra as an inset. The overall shape of the curves was maintained despite the preparation temperature showing the typical emission spectra of CN materials. Some variations of PL intensity were verified, as easily observed in Fig. 6b,

which is attributed to a modification of the electronic structure [50]. Furthermore, as it can be seen in the inset of Fig. 6b, there were slight wavelength deviations and an increase in the contribution of the lower-wavelength emissions. Bathochromic shifts were detected from lower to higher preparation temperatures and are typically associated with different crystalline arrangements and higher content of structural defects. To study this further, deconvolution of the PL signal was performed and presented in Figure S1.

The PL spectra of these materials consist of four main peaks of Gaussian nature (P1-4). The higher wavelength peaks are attributed to transitions between $\sigma*$ bonds to nitrogen lone pair states (P1), followed by less energetic and $\pi*$ to LP (P2) and to π bonds (P3) [48,51]. The lower wavelength peak (P4) can be owed to terminal functional bonds with high electro-affinity [50,51]. The prepared materials showed a general tendency from lower to higher preparation temperature: reduced contributions of the P1 peaks and intensification of the higher wavelength P4 peaks. From CN-450 to CN-650, there is a variation from 31.5 and 15.1 % to 23.4 and 46.3 %, respectively, for the most (P1) and least (P4) energetic peaks (Figure S1). This is in agreement with the previous characterisation, as the material prepared at the highest temperature shows the most defective structure. CN-550 is shown as the material with a more balanced ratio between the highest/lowest energetic (P1/P4) peaks in the group.

3.2. OER performance of CN

3.2.1. OER conditions

The electrochemical activity of the prepared materials was assessed for OER in different conditions, compared to the bare support and reference IrO$_2$, also immobilised on nickel foam. The optimisation of reaction conditions was performed by varying the pH value of the electrolyte and catalyst loading on the nickel foam support. In addition, the CN materials required persistent activation by cyclic voltammetry (CV) scans to achieve steady-state conditions for constant OER performance, as depicted in Figure S2.

In Fig. 7 it is possible to observe the anodic polarisation curves for the CN-550 material, following 250 CV activation cycles under alkaline, neutral, and acid environments (Fig. 7a) and using different catalyst loads on the nickel foam (Fig. 7b). At an alkaline pH, the lowest OER overpotential at 10 mA cm^{-2} of 355 mV was achieved, while at acid and neutral pH, higher overpotentials of 370 and 720 were required, respectively. The CN-550 material showed a good electrocatalytic performance at both acidic and alkaline pH, which was expected according to previous works reported with other CN-based materials [52,53], most probably owing to the amphoteric nature of CN [29,54]. One major difference between alkaline and acidic OER is the large pre-oxidation peak centred at 1.45 V *vs* NHE (19 mA cm^{-2}), which can be related to the electrode nature and its interaction with the reactive media [55,56]. The poor OER efficiency observed for near-neutral conditions might be caused by the system complexity derived from the possibility of occurring both alkaline and acid reaction pathways [55] and the difficulty of water electrolytic disassociation at neutral pH [57].

Then, the best OER properties were found for a catalyst load of 1.00 mg cm^{-2}. Higher CN content could induce the blockage of active sites. Poor loading may hinder charge transfer in the electrode surface [58].

The remaining studies were performed after 250 CV cycles for a proper electrochemically active electrode [59,60]. The activation voltammograms are shown in Figure S2, indicating that the current density keeps increasing until the 100th cycle, whereas there is a stabilisation reaching steady-state conditions until the 250th cycle. This requirement of activation cycles is usual of hydrophilic materials, where the applied potential favours the contact between electrolyte and electrode [61]. Hence, the following results are shown after 250 CV cycles, at catalyst's dosage of 1.00 mg cm^{-2} and with alkaline pH media.
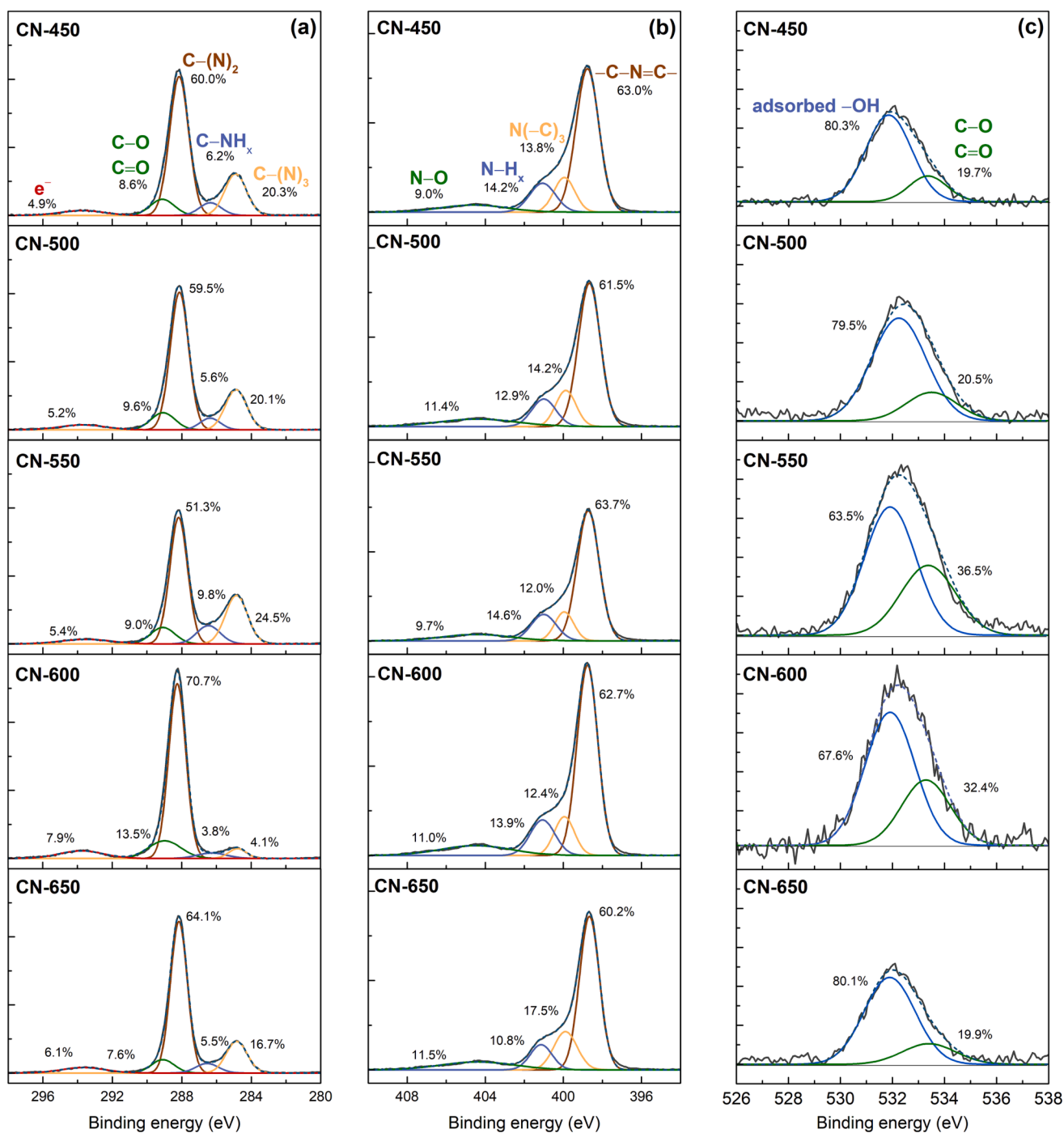
Fig. 5. XPS deconvolution of the **(a)** C 1s, **(b)** N 1s and **(c)** O 1s bands for the CN electrocatalysts.

3.2.2. Anodic polarisation curves

Looking into the linear voltammogram profiles, after 250 CV activation cycles, in Fig. 8a, it is possible to observe that the prepared electrocatalysts showed improved OER performance, compared to the nickel foam support, while particular materials revealed an even better electrocatalytic activity than IrO_2. The CN materials ensured pre-oxidation peaks at lower potentials than their onset values. The pre-oxidation peaks of the prepared materials were registered at a lower potential (1.44 – 1.46 V *vs* RHE) than that of the bare nickel foam (1.47 V *vs* RHE). The lowest OER overpotential at 10 mA cm^{-2} was registered for the CN-550 material (355 mV), surpassing that of the benchmark IrO_2 electrode (380 mV). Additionally, the remaining materials showed smaller or akin overpotential than the reference IrO_2, revealing that the

CN materials are, in fact, stimulating the electrocatalytic OER process through rapid electron transfer. There are only few references which have surpassed IrO_2 performance and those are based on metal-based catalysts [62,63]. Indeed, an up-to-date review states there is no metal-free catalyst competing to IrO_2 [64]. Thus, this study permits to optimize IrO_2 performance by using unexpensive and metal-free CN.

Moreover, the Tafel slopes (Fig. 8b) were calculated to investigate the intrinsic activity of the prepared catalysts [62]. It is known that a smaller Tafel slope is related to a greater driving force for enhanced catalytic activity. Most CN materials depicted a smaller Tafel slope value (46.8, 57.1, 65.6, 68.4 mV dec^{-1} for CN-550, CN-600, CN-500 and CN-450, respectively) than the reference electrocatalyst (79.0 mV dec^{-1}). This confirms the electrochemical proficiency of the prepared materials
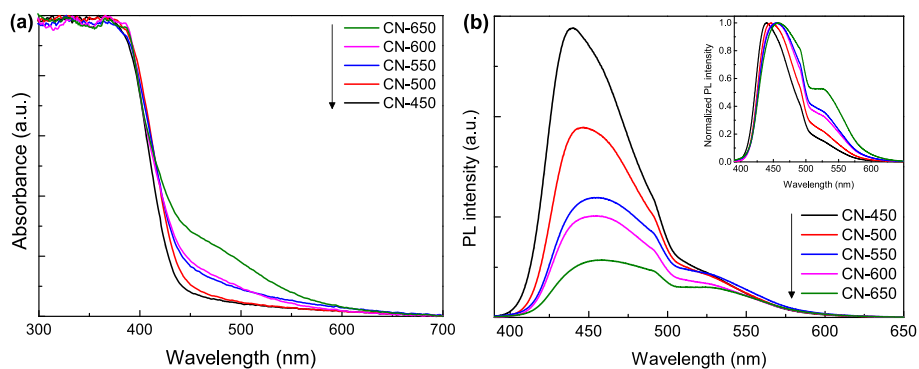
Fig. 6. (a) UV–vis absorbance and **(b)** steady-state PL emission spectra (with an inset for normalised PL) for the prepared CN electrocatalysts.
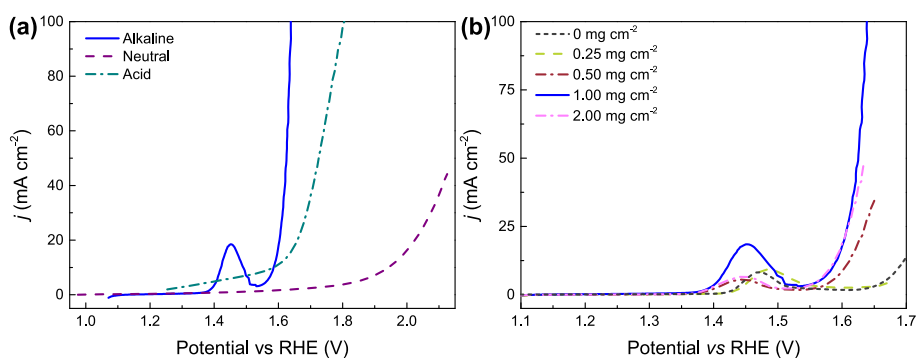

Fig. 7. Anodic polarisation curves using CN-550 **(a)** under different pH (with a catalyst load of 1.00 mg cm^{-2}) and **(b)** various loadings onto the nickel foam (alkaline media).
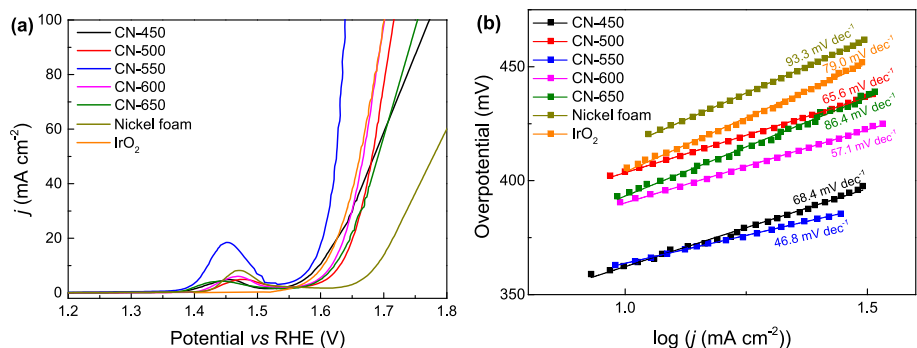

Fig. 8. (a) Anodic polarisation curves of the prepared catalysts and **(b)** corresponding Tafel slopes.

for the OER process. The CN-650 had a slightly higher Tafel slope (86.4 mV dec^{-1}) which can be attributed to the high degree of thermal exfoliation that could have damaged the active sites.

Overall, the superior electrocatalytic activity of CN-550 can be ascribed to the pronounced structural distortion seen by the highest I_D/I_G ratio in Raman spectroscopy, the largest content of oxygen in its elemental composition and the large distribution of terminal functional groups, suggested by XPS and PL. Specifically, oxygen-rich catalysts have shown promising OER ability as oxidic groups which can provide favourable surface adsorption and electrochemical active sites [65–67].

Previous works concerning electrocatalytic OER have been found with metal-free CN materials (alone or combined with other carbon materials) and are listed in **Table S1**. Comparison between Tafel slope and overpotential at 10 mA cm^{-2} of prepared materials to state-of-the-art CN-derived catalysts can also be found in **Table S1**. Different modifications have been performed to improve the performance of these catalysts, such as doping, conjugation with other conductive materials

or co-polymerisation procedures. It is noteworthy to highlight that those works were predominantly carried out using a KOH solution as the electrolyte. This abides well with our work, as the prepared materials performed best at an alkaline pH.

The literature reports of metal-free CN show modified materials, with the incorporation of graphene-derivatives [53,68–73], non-metal doping [74–77], co-polymerised catalysts [78–81] or even with a rearranged skeletal structure by acid-etching [82] or by forming nanotubes [83], a mesoporous model [84] or quantum dots [85]. Moreover, as can be seen in **Table S1**, where the Tafel slope and overpotential at 10 mA cm^{-2} are compared, the CN-550 catalyst proved to be one of the best-performing OER metal-free CN catalysts in the literature, particularly in terms of Tafel slope, indicating a quicker OER kinetics. For instance, the catalyst prepared by Yan *et al.* showed a very similar electrochemical activity (higher Tafel slope at 50.6 mV dec^{-1} but a lower overpotential of 120 mV) and was also synthesised using urea as a precursor although modified by boron-doping [68]. Kim *et al.* synthesised a CN material by

thermal calcination of melamine, followed by ultrasound–assisted exfoliation and freeze-casting to covalently combine the CN with a graphene aerogel [86]. Compared to this work, the bifunctional electrocatalyst prepared by Kim *et al.* showed a lower overpotential of 260 mV at 10 mA cm^{-2}, but a higher Tafel slope of 68 mV dec^{-1} [86]. Despite these optimisation techniques, our work with a simple one-pot preparation procedure yields comparable electrochemical results to those published in the literature.

3.2.3. Electrochemical characterisation

The values of C_{dl} (Fig. 9a) were determined at the non-faradaic region of the polarisation curves through the slope of current density variation at different voltammogram scan rates (Figure S3). Current density variation ($|\Delta j|$) is calculated by the difference between the anodic and cathodic currents ($j_a - j_c$) obtained at different scan rates. The value of C_{dl} is equivalent to half of that of the slope in Fig. 9a. The intrinsic catalytic performance can be assessed by the C_{dl}, with higher slopes being related to more active materials. Therefore, CN-550 shows a C_{dl} value of 358.5 µF cm^{-2}, which is 1.9 times higher than that of the bare nickel foam electrode. The electrochemical surface area (ECSA) is another important parameter to investigate the OER catalytic performance. The presence of the CN catalysts substantially increased the ECSA compared to the nickel foam. The effective ECSA of CN-550 was determined to be 9.0 cm^2, which is larger than that of the remaining materials. This could be attributed to a balance between amorphous and crystalline surfaces, along with distinct chemical characteristics that facilitate strong adherence to the nickel foam support and increased accessibility of electrochemically active sites.

Then, EIS studies were carried out to assess the charge transfer system at the electrode interface. An equivalent circuit model was fitted to the impedance measurements. The Nyquist plots (Fig. 9b) corroborate the improved OER rate of the CN electrocatalysts owing to the small arc radius of the fitted model, which is directly related to reduced charge transfer resistance [87]. Notably, the CN-550 depicts the shortest EIS arc, with a resistance to charge transfer (R_{CT}) of 1.76 Ω, correlated to its highest electrochemical OER ability.

Table 3 summarises the electrochemical water oxidation properties in the alkaline electrolyte solution for the five prepared electrocatalysts as well as reference IrO$_2$ and bare nickel foam. The anodic polarisation curves (Fig. 8a) previously investigated are herein fully characterised in terms of the pre-oxidation potential, overpotential (η) at 10 and 100 mA cm^{-2} and Tafel slope, alongside the values for double-layer capacitance (C_{dl}), electrochemical surface area (ECSA) and charge transfer resistance (R_{CT}).

3.2.4. Electrode galvanostatic stability

The electrochemical stabilities of the CN-550 and IrO$_2$ catalysts were investigated by conducting chronopotentiometric measurements at 10, 50 and 100 mA cm^{-2} (Fig. 10). This represents a more accurate stability

Table 3
Summary of OER results for the studied electrocatalysts.

Catalyst	CN-450	CN-500	CN-550	CN-600	CN-650	Nickel foam	IrO$_2$
Pre-oxidation peak potential (V)	1.46	1.47	1.45	1.46	1.44	1.47	–
η_{10} (mV)	370	400	355	390	390	460	380
η_{100} (mV)	540	490	400	470	520	660	470
Tafel slope (mV dec^{-1})	68.4	65.6	46.8	57.1	86.4	93.3	79.0
C_{dl} (µF cm^{-2})	240.4	254.5	358.5	264.2	207.0	184.9	–
ECSA (cm^2)	6.0	6.4	9.0	6.6	5.2	4.6	–
R_{CT} (Ω)	3.47	2.49	1.76	2.54	3.59	5.96	4.42

measurement as the typical 10 mA cm^{-2} tests [63,64] The overpotential outputs of the CN catalyst remained considerably stable, with a detriment smaller than 4.9 % of the initial overpotential during the continuous measurement period of 15 h at each applied current density. On the other hand, IrO$_2$ showed a reasonably stable activity at 10 mA cm^{-2}; however, under higher current densities, the overpotential values increased significantly (around 15 % after 15 h compared to the initial value). Additionally, the chronoamperometric study for Ni foam alone shows very high overpotentials but with a solid endurance to the applied current intensities, proving its resilience as an effective support for CN immobilisation. These results indicate excellent electrochemical stability of the CN electrocatalyst, particularly when compared to the poor stability of the reference material.

The CN-550 material was analysed after a long-term chronoamperometry experiment. Several CV cycles were performed, performed, and the results obtained after 250 cycles are portrayed in Fig. 10b, compared to the initial CV. It is possible to observe a small reduction of the pre-oxidation peak intensity, as well as a slight increase of the overpotential up to 370 mV at 10 mA cm^{-2}. Impedance studies were performed with the spent catalyst, depicting a small augmentation of the arc radius in the Nyquist plot (Fig. 10c). The loss of electrochemical activity can be attributed to a variety of factors. For instance, PL spectra (Fig. 10d) show a quenched intensity, which can be associated with blocked active centres that hinder electron transfer, but the same shape of the emission curve is maintained, thus suggesting that the core structure of CN-550 is preserved [88,89]. Chemical structure analyses - FTIR and XPS (Fig. 10e and Fig. 10f, respectively) - show a wide gain of oxygen-related groups, *viz.* the strong IR band at 3500 cm^{-1} of adsorbed –OH [90] and the intense O 1s XPS peak [91]. Also, the reduced intensity of IR bands in the 600 – 2000 cm^{-1} range can be attributed to the oxygen moieties resulting from the prolonged OER assay. The used catalyst also shows the previously inexistent O KLL XPS peak, which is owed to Auger delocalised electrons derived from newly formed surface defects [49]. It is important to note that XPS is a surface-sensitive
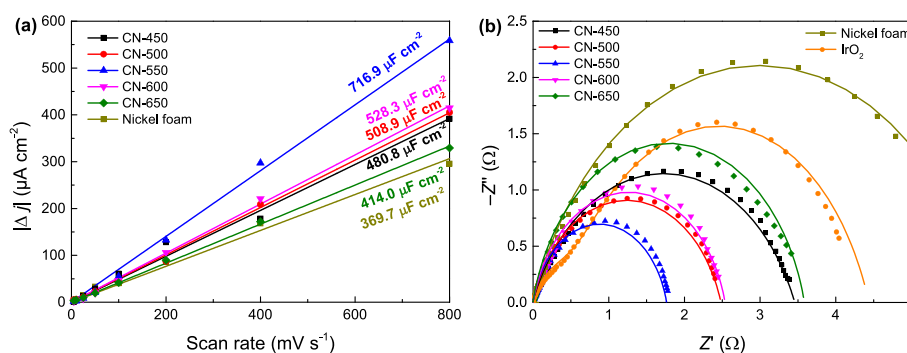

Fig. 9. (a) Plot of current density variation ($|\Delta j| = j_a - j_c$) *versus* voltammogram scan rates, whose slope corresponds to the double of the double-layer capacitance (C_{dl}) and (b) Nyquist plots to obtain the charge transfer resistance (R_{CT}) of the prepared catalysts.
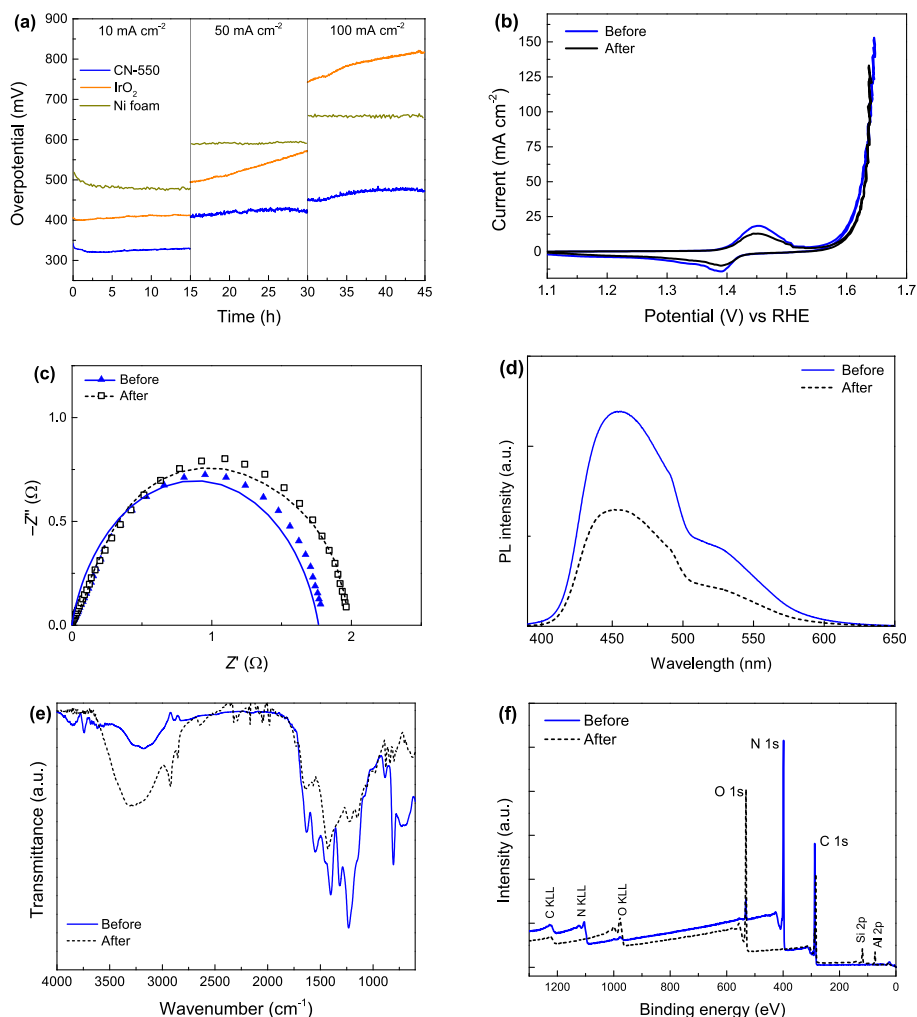
Fig. 10. (a) Chronopotentiometry of the CN-550, IrO$_2$, and bare Ni foam electrodes at different current densities and comparison of CN-550 before and after the stability test by **(b)** CV, **(c)** EIS, **(d)** PL emission spectroscopy, **(e)** FTIR and **(f)** XPS survey.

technique, and it shows that at the surface the nitrogen groups are not observed most probably due to the over-oxidation of the surface caused by the extensive OER chronoamperometry experiment. In sum, the spent material shows a slight loss of electrocatalytic activity; however, it remains fairly electrochemically-active.

4. Conclusions

The g-C$_3$N$_4$ materials prepared from the thermal polymerisation of urea showed great potential as electrocatalysts for OER, owing to their unique electronic structure and high stability. Characterisation techniques were useful in understanding the effect of the preparation temperature on the properties of the resulting CN materials and their corresponding OER performances. The specific crystalline organisation and structural arrangement (smallest I_D/I_G ratio from Raman spectroscopy), appropriate porosity and adequate composition in terminal functional groups (observed by elemental analysis and PL deconvolution) endowed the material treated at 550 °C (*i.e.*, CN-550) to achieve outstanding OER results: a low overpotential of 355 mV at 10 mA cm^{-2} and a Tafel slope of 46.8 mV dec^{-1}. Electrochemical impedance and capacitance studies (EIS and C_{dl}) corroborated the electrocatalytic behaviour of this catalyst as it presented the smallest Nyquist arc and the highest double-layer capacitance. Moreover, the chronoamperometric studies showed that the fabricated CN-550 electrodes were stable under various current densities for up to 45 h. Despite this, future research should be focused on gaining deeper insights into the catalytic

mechanism of g-C$_3$N$_4$-derived materials and on scaling-up processes.

CRediT authorship contribution statement

André Torres-Pinto: . **Aida M. Díez:** . **Cláudia G. Silva:** Writing – review & editing, Project administration, Funding acquisition. **Joaquim L. Faria:** Writing – review & editing, Project administration, Funding acquisition. **M. Ángeles Sanromán:** . **Adrián M.T. Silva:** Writing – review & editing, Project administration, Funding acquisition. **Marta Pazos:** Writing – review & editing, Resources, Project administration, Funding acquisition.

Declaration of competing interest

The authors declare that they have no known competing financial interests or personal relationships that could have appeared to influence the work reported in this paper.

Data availability

Data will be made available on request.

Acknowledgements

Appendix A. Supplementary material

Supplementary data to this article can be found online at https://doi. org/10.1016/j.fuel.2023.130575.

References

[1] Boretti A, Banik BK. Advances in Hydrogen Production from Natural Gas Reforming. Adv Energy Sustain Res 2021;2:2100097.

[2] Peng Y, Jiang K, Hill W, Lu Z, Yao H, Wang H. Large-Scale, Low-Cost, and High-Efficiency Water-Splitting System for Clean H_2 Generation. ACS Appl Mater Interfaces 2019;11:3971–7.

[3] Bockris JOM. The origin of ideas on a Hydrogen Economy and its solution to the decay of the environment. Int J Hydrog Energy 2002;27:731–40.

[4] Song J, Wei C, Huang Z-F, Liu C, Zeng L, Wang X, et al. A review on fundamentals for designing oxygen evolution electrocatalysts. Chem Soc Rev 2020;49:2196–214.

[5] Karmakar A, Karthick K, Sankar SS, Kumaravel S, Madhu R, Kundu S. A vast exploration of improvising synthetic strategies for enhancing the OER kinetics of LDH structures: A review. J Mater Chem A 2021;9:1314–52.

[6] Anantharaj S, Ede SR, Sakthikumar K, Karthick K, Mishra S, Kundu S. Recent Trends and Perspectives in Electrochemical Water Splitting with an Emphasis on Sulfide, Selenide, and Phosphide Catalysts of Fe Co, and Ni: A Review. ACS Catal 2016;6:8069–97.

[7] Li A, Sun Y, Yao T, Han H. Earth-Abundant Transition-Metal-Based Electrocatalysts for Water Electrolysis to Produce Renewable Hydrogen. Chem Eur J 2018;24: 18334–55.

[8] Liu B, Sun Y, Liu L, Xu S, Yan X. Advances in Manganese-Based Oxides Cathodic Electrocatalysts for Li–Air Batteries. Adv Funct Mater 2018;28:1704973.

[9] Lv L, Yang Z, Chen K, Wang C, Xiong Y. 2D Layered Double Hydroxides for Oxygen Evolution Reaction: From Fundamental Design to Application. Adv Energy Mater 2019;9:1803358.

[10] Wang HF, Chen L, Pang H, Kaskel S, Xu Q. MOF-derived electrocatalysts for oxygen reduction, oxygen evolution and hydrogen evolution reactions. Chem Soc Rev 2020;49:1414–48.

[11] Jiang W, Tao Y, Ma J, Liu X, Zhu S, Hao W, et al. Interfacial Electronic Modulation on Nickel Cobaltite/Black Phosphorus Heterostructures for Boosting the Electrocatalytic Oxygen Evolution Reaction. ACS Sustain Chem Eng 2023;11: 6629–40.

[12] Hu C, Dai L. Carbon-Based Metal-Free Catalysts for Electrocatalysis beyond the ORR. Angew Chem Int Ed 2016;55:11736–58.

[13] Zhao JW, Shi ZX, Li CF, Ren Q, Li GR. Regulation of Perovskite Surface Stability on the Electrocatalysis of Oxygen Evolution Reaction. ACS Mater Lett 2021;3:721–37.

[14] Yun TG, Sim Y, Lim Y, Kim D, An JS, Lee H, et al. Surface dissolution and amorphization of electrocatalysts during oxygen evolution reaction: Atomistic features and viewpoints. Mater Today 2022;58:221–37.

[15] Wang J, Kong H, Zhang J, Hao Y, Shao Z, Ciucci F. Carbon-based electrocatalysts for sustainable energy applications. Prog Mater Sci 2021;116:100717.

[16] Sun J, Xu J, Grafmueller A, Huang X, Liedel C, Algara-Siller G, et al. Self-assembled carbon nitride for photocatalytic hydrogen evolution and degradation of *p*-nitrophenol. Appl Catal B-Environ 2017;205:1–10.

[17] Li Y, Gu M, Shi T, Cui W, Zhang X, Dong F, et al. Carbon vacancy in C_3N_4 nanotube: Electronic structure, photocatalysis mechanism and highly enhanced activity. Appl Catal B-Environ 2020;262:118281.

[18] Guo Y, Huang S, Guo Y, Ye Z, Nan J, Zhou Q, et al. Efficient degradation of organic pollutants by enhanced interfacial internal electric field induced via various crystallinity carbon nitride homojunction. Appl Catal B-Environ 2022;312:121388.

[19] Niu H, Wan X, Wang X, Shao C, Robertson J, Zhang Z, et al. Single-Atom Rhodium on Defective g-C_3N_4: A Promising Bifunctional Oxygen Electrocatalyst. ACS Sustain Chem Eng 2021;9:3590–9.

[20] Lee CH, Jun B, Lee SU. Metal-Free Oxygen Evolution and Oxygen Reduction Reaction Bifunctional Electrocatalyst in Alkaline Media: From Mechanisms to Structure-Catalytic Activity Relationship. ACS Sustain Chem Eng 2018;6:4973–80.

[21] Jo WK, Moru S, Tonda S. Cobalt-Coordinated Sulfur-Doped Graphitic Carbon Nitride on Reduced Graphene Oxide: An Efficient Metal-(N, S)-C-Class Bifunctional Electrocatalyst for Overall Water Splitting in Alkaline Media. ACS Sustain Chem Eng 2019;7:15373–84.

[22] Xia S, Guo W, Cai N, Sun L, Zhou H, Lu W, et al. Synthesis and application in oxygen reduction reaction of N-doping porous graphitic carbon from biomass waste. Fuel Process Technol 2021;224:107028.

[23] Wu J, Liu Z, Lin X, Jiang E, Zhang S, Huo P, et al. Breaking through water-splitting bottlenecks over carbon nitride with fluorination. Nature Commun 2022;13:6999.

[24] Lv X, Wei W, Wang H, Huang B, Dai Y. Holey graphitic carbon nitride (g-CN) supported bifunctional single atom electrocatalysts for highly efficient overall water splitting. Appl Catal B-Environ 2020;264:118521.

[25] Ren R, Liu G, Kim JY, Ardhi REA, Tran MX, Yang W, et al. Photoactive g-C_3N_4/ CuZIF-67 bifunctional electrocatalyst with staggered p-n heterojunction for rechargeable Zn-air batteries. Appl Catal B-Environ 2022;306:121096.

[26] Liu J, Wang C, Sun H, Wang H, Rong F, He L, et al. CoO_x/CoN_y nanoparticles encapsulated carbon-nitride nanosheets as an efficiently trifunctional electrocatalyst for overall water splitting and Zn-air battery. Appl Catal B-Environ 2020;279:119407.

[27] U.A. Asif, T. Noor, E. Pervaiz, N. Iqbal, N. Zaman, LSTN ($La_{0.4}Sr_{0.4}Ti_{0.9}Ni_{0.1}O_{3-\&}$) perovskite and graphitic carbon nitride (g-C_3N_4) hybrids as a bifunctional electrocatalyst for water-splitting applications, J. Alloys Compd., 939 (2023) 168668.

[28] M. Benedet, G. Andrea Rizzi, A. Gasparotto, N. Gauquelin, A. Orekhov, J. Verbeeck, C. Maccato, D. Barreca, Functionalization of graphitic carbon nitride systems by cobalt and cobalt-iron oxides boosts solar water oxidation performances, Appl. Surf. Sci., 618 (2023) 156652.

[29] Torres-Pinto A, Silva CG, Faria JL, Silva AMT. The effect of precursor selection on the microwave-assisted synthesis of graphitic carbon nitride. Catal Today 2023; 424:113868.

[30] Lima MJ, Silva AMT, Silva CG, Faria JL. Graphitic carbon nitride modified by thermal, chemical and mechanical processes as metal-free photocatalyst for the selective synthesis of benzaldehyde from benzyl alcohol. J Catal 2017;353:44–53.

[31] Gu Q, Gao Z, Zhao H, Lou Z, Liao Y, Xue C. Temperature-controlled morphology evolution of graphitic carbon nitride nanostructures and their photocatalytic activities under visible light. RSC Adv 2015;5:49317–25.

[32] Fina F, Callear SK, Carins GM, Irvine JTS. Structural Investigation of Graphitic Carbon Nitride via XRD and Neutron Diffraction. Chem Mater 2015;27:2612–8.

[33] Wu P, Wang J, Zhao J, Guo L, Osterloh FE. Structure defects in g-C_3N_4 limit visible light driven hydrogen evolution and photovoltage. J Mater Chem A 2014;2: 20338–44.

[34] Papailias I, Giannakopoulou T, Todorova N, Demotikali D, Vaimakis T, Trapalis C. Effect of processing temperature on structure and photocatalytic properties of g-C_3N_4. Appl Surf Sci 2015;358:278–86.

[35] Wang H, Zhang X, Xie J, Zhang J, Ma P, Pan B, et al. Structural distortion in graphitic-C_3N_4 realizing an efficient photoreactivity. Nanoscale 2015;7:5152–6.

[36] Ribeiro RS, Silva AMT, Pastrana-Martínez LM, Figueiredo JL, Faria JL, Gomes HT. Graphene-based materials for the catalytic wet peroxide oxidation of highly concentrated 4-nitrophenol solutions. Catal Today 2015;249:204–12.

[37] Wang M, Wu Z, Dai L. Graphitic carbon nitrides supported by nitrogen-doped graphene as efficient metal-free electrocatalysts for oxygen reduction. J Electroanal Chem 2015;753:16–20.

[38] Pastrana-Martínez LM, Morales-Torres S, Likodimos V, Falaras P, Figueiredo JL, Faria JL, et al. Role of oxygen functionalities on the synthesis of photocatalytically active graphene–TiO2 composites. Appl Catal B-Environ 2014;158–159:329–40.

[39] Hernández-Torres J, Gutierrez-Franco A, González PG, García-González L, Hernandez-Quiroz T, Zamora-Peredo L, et al. Photoluminescence and Raman Spectroscopy Studies of Carbon Nitride Films. J Spectrosc 2016;2016:5810592.

[40] Gashi A, Parmentier J, Fioux P, Marsalek R. Tuning the C/N Ratio of C-Rich Graphitic Carbon Nitride (g-C3N4) Materials by the Melamine/Carboxylic Acid Adduct Route. Chem Eur J 2022;28:e202103605.

[41] Addie AJ, Ismail RA, Mohammed MA. Amorphous carbon nitride dual-function anti-reflection coating for crystalline silicon solar cells. Sci Rep 2022;12:9902.

[42] Kotbi A, Benyoussef M, Ressami EM, Lejeune M, Lakssir B, Jouiad M. Gas Sensors Based on Exfoliated g-C_3N_4 for CO_2 Detection. Chemosensors 2022;10:470.

[43] Zhao S, Fang J, Wang Y, Zhang Y, Zhou Y, Zhuo S. Synthesis of carbon nitride hollow microspheres with highly hierarchical porosity templated by poly (ionic liquid) for photocatalytic hydrogen evolution. Appl Organomet Chem 2020;34: e5474.

[44] Xiao X, Wang Y, Bo Q, Xu X, Zhang D. One-step preparation of sulfur-doped porous g-C_3N_4 for enhanced visible light photocatalytic performance. Dalton Trans 2020; 49:8041–50.

[45] Hellgren N, Haasch RT, Schmidt S, Hultman L, Petrov I. Interpretation of X-ray photoelectron spectra of carbon-nitride thin films: New insights from in situ XPS. Carbon 2016;108:242–52.

[46] Yan W, Yan L, Jing C. Impact of doped metals on urea-derived g-C3N4 for photocatalytic degradation of antibiotics: Structure, photoactivity and degradation mechanisms. Appl Catal B-Environ 2019;244:475–85.

[47] Kumar A, Kumar P, Joshi C, Manchanda M, Boukherroub R, Jain SL. Nickel Decorated on Phosphorous-Doped Carbon Nitride as an Efficient Photocatalyst for Reduction of Nitrobenzenes. Nanomaterials 2016;6:59.

[48] Zhang Y, Pan Q, Chai G, Liang M, Dong G, Zhang Q, et al. Synthesis and luminescence mechanism of multicolor-emitting g-C_3N_4 nanopowders by low temperature thermal condensation of melamine. Sci Rep 2013;3:1943.

[49] Da Silva ES, Moura NMM, Coutinho A, Dražić G, Teixeira BMS, Sobolev NA, et al. B-Cyclodextrin as a Precursor to Holey C-Doped g-C3N4 Nanosheets for Photocatalytic Hydrogen Generation. ChemSusChem 2018;11:2681–94.

[50] Jiao Y, Hu R, Wang Q, Fu F, Chen L, Dong Y, et al. Tune the Fluorescence and Electrochemiluminescence of Graphitic Carbon Nitride Nanosheets by Controlling the Defect States. Chem Eur J 2021;27:10925–31.

[51] Wang BB, Cheng QJ, Wang LH, Zheng K, Ostrikov K. The effect of temperature on the mechanism of photoluminescence from plasma-nucleated, nitrogenated carbon nanotips. Carbon 2012;50:3561–71.

[52] Yu Z, Li Y, Torres-Pinto A, LaGrow AP, Diaconescu VM, Simonelli L, et al. Single-atom Ir and Ru anchored on graphitic carbon nitride for efficient and stable

electrocatalytic/photocatalytic hydrogen evolution. Appl Catal B-Environ 2022; 310:121318.

[53] Peng Z, Yang S, Jia D, Da P, He P, Al-Enizi AM, et al. Homologous metal-free electrocatalysts grown on three-dimensional carbon networks for overall water splitting in acidic and alkaline media. J Mater Chem A 2016;4:12878–83.

[54] Torres-Pinto A, Sampaio MJ, Silva CG, Faria JL, Silva AMT. Metal-free carbon nitride photocatalysis with *in situ* hydrogen peroxide generation for the degradation of aromatic compounds. Appl Catal B-Environ 2019;252:128–37.

[55] Fornaciari JC, Weng L-C, Alia SM, Zhan C, Pham TA, Bell AT, et al. Mechanistic understanding of pH effects on the oxygen evolution reaction. Electrochim Acta 2022;405:139810.

[56] Hu X, Tian X, Lin Y-W, Wang Z. Nickel foam and stainless steel mesh as electrocatalysts for hydrogen evolution reaction, oxygen evolution reaction and overall water splitting in alkaline media. RSC Adv 2019;9:31563–71.

[57] Xu Y, Wang C, Huang Y, Fu J. Recent advances in electrocatalysts for neutral and large-current-density water electrolysis. Nano Energy 2021;80:105545.

[58] Yu L, Sun S, Li H, Xu ZJ. Effects of catalyst mass loading on electrocatalytic activity: An example of oxygen evolution reaction. Fundam Res 2021;1:448–52.

[59] Zhang R, van Straaten G, di Palma V, Zafeiropoulos G, van de Sanden MCM, Kessels WMM, et al. Electrochemical Activation of Atomic Layer-Deposited Cobalt Phosphate Electrocatalysts for Water Oxidation. ACS Catal 2021;11:2774–85.

[60] Hong S, Díez AM, Adeyemi AN, Sousa JPS, Salonen LM, Lebedev OI, et al. Deep Eutectic Solvent Synthesis of Perovskite Electrocatalysts for Water Oxidation, ACS Appl. Mater Interfaces 2022;14:23277–84.

[61] Y. Han, C. Yu, H. Huang, Q. Wei, J. Dong, L. Chen, J. Qiu, Controllable surface reconstruction of copper foam for electrooxidation of benzyl alcohol integrated with pure hydrogen production, SmartMat, (2023) e1206.

[62] Ehsan MA, Babar N-U-A. Straightforward Preparation of Fe-Based Electrocatalytic Films at Various Substrates for IrO2-like Water Oxidation Activity. Energy Fuel 2023;37:3934–41.

[63] Lu X-F, Gu L-F, Wang J-W, Wu J-X, Liao P-Q, Li G-R. Bimetal-Organic Framework Derived CoFe2O4/C Porous Hybrid Nanorod Arrays as High-Performance Electrocatalysts for Oxygen Evolution Reaction. Adv Mater 2017;29:1604437.

[64] Wang R, Zhang Z, Suo J, Liao L, Li L, Yu Z, et al. Exploring Metal-Free Ionic Covalent Organic Framework Nanosheets as Efficient OER Electrocatalysts Via Cationic-Π Interactions. Chem Eng J 2023;478:147403.

[65] Ding K, Ye Y, Hu J, Zhao L, Jin W, Luo J, et al. Aerophilic Triphase Interface Tuned by Carbon Dots Driving Durable and Flexible Rechargeable Zn-Air Batteries. Nano-Micro Lett 2023;15:28.

[66] Zance SS, Ravichandran S. Electrochemical surface modification of carbon for enhanced water electrolysis. Appl Phys A 2019;125:456.

[67] Zhang W, Xu C-H, Zheng H, Li R, Zhou K. Oxygen-Rich Cobalt–Nitrogen–Carbon Porous Nanosheets for Bifunctional Oxygen Electrocatalysis. Adv Funct Mater 2022;32:2200763.

[68] Yan Q, Huang G-F, Li D-F, Zhang M, Pan A-L, Huang W-Q. Facile synthesis and superior photocatalytic and electrocatalytic performances of porous B-doped g-C3N4 nanosheets. J Mater Sci Technol 2018;34:2515–20.

[69] Choi H, Surendran S, Sim Y, Je M, Janani G, Choi H, et al. Enhanced electrocatalytic full water-splitting reaction by interfacial electric field in 2D/2D heterojunction. Chem Eng J 2022;450:137789.

[70] Li B, Fang Q, Si Y, Huang T, Huang W-Q, Hu W, et al. Ultra-thin tubular graphitic carbon Nitride-Carbon Dot lateral heterostructures: One-Step synthesis and highly efficient catalytic hydrogen generation. Chem Eng J 2020;397:125470.

[71] Ahsan MA, He T, Eid K, Abdullah AM, Curry ML, Du A, et al. Tuning the Intermolecular Electron Transfer of Low-Dimensional and Metal-Free BCN/C60 Electrocatalysts via Interfacial Defects for Efficient Hydrogen and Oxygen Electrochemistry. J Am Chem Soc 2021;143:1203–15.

[72] Lei H, Cui M, Huang Y. S-Doping Promotes Pyridine Nitrogen Conversion and Lattice Defects of Carbon Nitride to Enhance the Performance of Zn–Air Batteries. ACS Appl Mater Interfaces 2022;14:34793–801.

[73] Tian J, Liu Q, Asiri AM, Alamry KA, Sun X. Ultrathin Graphitic C3N4 Nanosheets/ Graphene Composites: Efficient Organic Electrocatalyst for Oxygen Evolution Reaction. ChemSusChem 2014;7:2125–30.

[74] Han E-X, Li Y-Y, Wang Q-H, Huang W-Q, Luo L, Hu W, et al. Chlorine doped graphitic carbon nitride nanorings as an efficient photoresponsive catalyst for water oxidation and organic decomposition. J Mater Sci Technol 2019;35: 2288–96.

[75] Shinde SS, Yu J-Y, Song J-W, Nam Y-H, Kim D-H, Lee J-H. Highly active and durable carbon nitride fibers as metal-free bifunctional oxygen electrodes for flexible Zn–air batteries. Nanoscale Horiz 2017;2:333–41.

[76] Li Y-Y, Zhou B-X, Zhang H-W, Ma S-F, Huang W-Q, Peng W, et al. Doping-induced enhancement of crystallinity in polymeric carbon nitride nanosheets to improve their visible-light photocatalytic activity. Nanoscale 2019;11:6876–85.

[77] Shiravani F, Tashkhourian J, Haghighi B. One-step synthesis of graphitic carbon-nitride doped with black-red phosphorus as a novel, efficient and free-metal bifunctional catalyst and its application for electrochemical overall water splitting, Sustain. Energy Fuels 2021;5:3229–39.

[78] Liu J, Wang C, Song Y, Zhang S, Zhang Z, He L, et al. Two-dimensional triazine-based porous framework as a novel metal-free bifunctional electrocatalyst for zinc-air batty. J Colloid Interface Sci 2021;591:253–63.

[79] Desalegn BZ, Jadhav HS, Seo JG. Highly Efficient g-C3N4 Nanorods with Dual Active Sites as an Electrocatalyst for the Oxygen Evolution Reaction. ChemCatChem 2019;11:2870–8.

[80] Ma S-F, Wei Z-X, Huang W-Q, Li Y-Y, Xiao S, Liu Z-K, et al. Protonated supramolecular complex-induced porous graphitic carbon nitride nanosheets as bifunctional catalyst for water oxidation and organic pollutant degradation. J Mater Sci 2019;54:7637–50.

[81] Li Y-Y, Si Y, Zhou B-X, Huang W-Q, Hu W, Pan A, et al. Strategy to boost catalytic activity of polymeric carbon nitride: synergistic effect of controllable in situ surface engineering and morphology. Nanoscale 2019;11:16393–405.

[82] Zhang H-W, Lu Y-X, Li B, Huang G-F, Zeng F, Li Y-Y, et al. Acid-induced topological morphology modulation of graphitic carbon nitride homojunctions as advanced metal-free catalysts for OER and pollutant degradation. J Mater Sci Technol 2021; 86:210–8.

[83] Ma T, Bai J, Wang Q, Li C. The novel synthesis of a continuous tube with laminated g-C3N4 nanosheets for enhancing photocatalytic activity and oxygen evolution reaction performance. Dalton Trans 2018;47:10240–8.

[84] Wahab MA, Joseph J, Atanda L, Sultana UK, Beltramini JN, Ostrikov K, et al. Nanoconfined Synthesis of Nitrogen-Rich Metal-Free Mesoporous Carbon Nitride Electrocatalyst for the Oxygen Evolution Reaction. ACS Appl Energy Mater 2020;3: 1439–47.

[85] Wang F, Wang Q, Wang S, Zhang K, Jia S, Chen J, et al. Water-Phase Lateral Interconnecting Quantum Dots as Free-Floating 2D Film Assembled by Hydrogen-Bonding Interactions to Acquire Excellent Electrocatalytic Activity. ACS Nano 2022;16:9049–61.

[86] Kim J, Tiwari AP, Choi M, Chen Q, Lee J, Novak TG, et al. Boosting bifunctional oxygen electrocatalysis of graphitic C3N4 using non-covalently functionalized non-oxidized graphene aerogels as catalyst supports. J Mater Chem A 2022;10: 15689–97.

[87] Alaghmandfard A, Ghandi K. A Comprehensive Review of Graphitic Carbon Nitride (g-C3N4)–Metal Oxide-Based Nanocomposites: Potential for Photocatalysis and Sensing. Nanomaterials 2022;12:294.

[88] Zhu S, Zhang J, Tang S, Qiao C, Wang L, Wang H, et al. Surface Chemistry Routes to Modulate the Photoluminescence of Graphene Quantum Dots: From Fluorescence Mechanism to Up-Conversion Bioimaging Applications. Adv Funct Mater 2012;22: 4732–40.

[89] Lu Z, Zhai X, Yi R, Li Z, Zhang R, Wei Q, et al. Photoluminescence Emission during Photoreduction of Graphene Oxide Sheets as Investigated with Single-Molecule Microscopy. J Phys Chem C 2020;124:7914–21.

[90] Luo R, Qian Z, Xing L, Du C, Yin G, Zhao S, et al. Re-Looking into the Active Moieties of Metal X-ides (X- = Phosph-, Sulf-, Nitr-, and Carb-) Toward Oxygen Evolution Reaction. Adv Funct Mater 2021;31:2102918.

[91] Fan K, Zou H, Lu Y, Chen H, Li F, Liu J, et al. Direct Observation of Structural Evolution of Metal Chalcogenide in Electrocatalytic Water Oxidation. ACS Nano 2018;12:12369–79.